

# Enhanced artificial intelligence-based diagnosis using CBCT with internal denoising: Clinical validation for discrimination of fungal ball, sinusitis, and normal cases in the maxillary sinus

Kyungsu Kim<sup>1,2\*</sup>, Chae Yeon Lim<sup>3\*</sup>, Joongbo Shin<sup>4</sup>, Myung Jin Chung<sup>1,2,3,5</sup>, Yong Gi Jung<sup>1,2,4†</sup>

<sup>1</sup>Medical AI Research Center, Research Institute for Future Medicine, Samsung Medical Center, Seoul, Republic of Korea

<sup>2</sup>Department of Data Convergence and Future Medicine, Sungkyunkwan University School of Medicine, Seoul, Republic of Korea

<sup>3</sup>Department of Medical Device Management and Research, SAIHST, Sungkyunkwan University, Seoul, Republic of Korea

<sup>4</sup>Department of Otorhinolaryngology-Head and Neck Surgery, Samsung Medical Center, Sungkyunkwan University School of Medicine, Seoul, Republic of Korea

<sup>5</sup>Department of Radiology, Samsung Medical Center, Sungkyunkwan University School of Medicine, Seoul, Republic of Korea

## Abstract

**Background and objective** The cone-beam computed tomography (CBCT) provides three-dimensional volumetric imaging of a target with low radiation dose and cost compared with conventional computed tomography, and it is widely used in the detection of paranasal sinus disease. However, it lacks the sensitivity to detect soft tissue lesions owing to reconstruction constraints. Consequently, only physicians with expertise in CBCT reading can distinguish between inherent artifacts or noise and diseases, restricting the use of this imaging modality. The development of artificial intelligence (AI)-based computer-aided diagnosis methods for CBCT to overcome the shortage of experienced physicians has attracted substantial attention. However, advanced AI-based diagnosis addressing intrinsic noise in CBCT has not been devised, discouraging the practical use of AI solutions for CBCT. We introduce the development of AI-based computer-aided diagnosis for CBCT considering the intrinsic imaging noise and evaluate its efficacy and implications.

**Methods** We propose an AI-based computer-aided diagnosis method using CBCT with a denoising module. This module is implemented before diagnosis to reconstruct the internal ground-truth full-dose scan corresponding to an input CBCT image and thereby improve the diagnostic performance. The proposed method is model agnostic and compatible with various existing and future AI-based denoising or diagnosis models.

**Results** The external validation results for the unified diagnosis of sinus fungal ball, chronic rhinosinusitis, and normal cases show that the proposed method improves the micro-, macro-average area under the curve, and accuracy by 7.4, 5.6, and 9.6% (from 86.2, 87.0, and 73.4 to 93.6, 92.6, and 83.0%), respectively, compared with a baseline while improving human diagnosis accuracy by 11% (from 71.7 to 83.0%), demonstrating technical differentiation and clinical effectiveness. In addition, the physician's ability to evaluate the AI-derived diagnosis results may be enhanced compared with existing solutions.

**Conclusion** This pioneering study on AI-based diagnosis using CBCT indicates that denoising can improve diagnostic performance and reader interpretability in images from the sinonasal area, thereby providing a new approach and direction to radiographic image reconstruction regarding the development of AI-based

\*These authors contributed equally to this work as co-first authors.

†Corresponding author (ent.jyg@gmail.com)

diagnostic solutions. Furthermore, we believe that the performance enhancement will expedite the adoption of automated diagnostic solutions using CBCT, especially in locations with a shortage of skilled clinicians and limited access to high-dose scanning.

## **1 Introduction**

### **1.1 Clinical value of cone-beam computed tomography as an alternative to conventional computed tomography**

Chronic rhinosinusitis (CRS) [1] is an inflammatory condition that affects from 2% to 16% of the population in the United States, being a significant disease that costs approximately \$10 billion in social expenses annually [2]. To reduce the social burden caused by CRS, accurate early diagnosis is crucial through methods such as sinonasal computed tomography (CT), which also allows the establishment of a surgical plan for endoscopic sinus surgery [3]. Conventional multidetector helical CT (MDCT) provides accurate high-quality coronal and sagittal images of the sinus [4], being a common diagnostic modality. However, MDCT has several drawbacks, including high cost, large installation area, and high radiation exposure [5]. In addition, MDCT is time-consuming when capturing and reassembling pictures, possibly causing adverse reactions such as claustrophobia in patients. Radiation exposure to radiation-sensitive organs, such as the eyes and thyroid gland, cannot be prevented during MDCT, restricting its repeated prescription around those organs.

Cone-beam CT (CBCT) is attracting attention as an image restoration technique that can overcome the shortcomings of MDCT. Compared with MDCT, CBCT features a shorter imaging time, less radiation dose, simpler reexamination, lower price, reduced installation area, and a simpler procedure even for claustrophobic patients owing to its open design. As CBCT employs an isotropic voxel to emit cone-shaped X-rays, they are irradiated simultaneously and not sequentially. Therefore, CBCT can reduce the dose with fewer scans while accurately reconstructing the patient's three-dimensional (3D) structures; that is, it retains the ratio between axes of the 3D volume from a target. In contrast, MDCT employs a linear X-ray beam and thus requires extensive imaging, resulting in large-dose exposure. The average dose used for MDCT imaging is 42% higher than that used for CBCT imaging (108 vs. 63  $\mu$ Sy) [6]. Owing to its expansive potential area, CBCT can reconstruct an MDCT image from an irradiated region with a single scan, thereby achieving low-dose, high-speed, and high-resolution imaging [7, 8].

### **1.2 Limitation of CBCT for widespread adoption in clinical use: Unreliable diagnosis in non-skeletal regions including soft tissues**

As CBCT uses cone X-ray beams rather than linear beams, it can provide the aforementioned advantages. Therefore, it replaces conventional MDCT and panoramic radiography, especially in dental practice. However, the CBCT principle contradicts the Fourier slice theorem from a technical perspective [9]. Filtered back projection [10] is the gold standard reconstruction method for MDCT images intended to address the inverse problem based on plane projection instead of cone-beam projection. Most commercially available image restoration systems for CBCT use filtered back-projection because no solution is available to completely solve the inversion of cone-beam projections completely. Unlike MDCT, CBCT has intrinsic artifacts [11] and noise because it reconstructs an image that is close to the ground truth but cannot reconstruct the true image. The imaging of soft tissues is particularly susceptible to these technical limitations. Combined with small radiation doses, CBCT provides inferior image resolution and distortion compared with MDCT when imaging soft tissues with lesions [12]. This limits the ability of CBCT to accurately diagnose inflammation in these tissues [13].

Various studies have claimed the need for educating clinicians to distinguish between disease and noise owing to the notable artifacts and noise on CBCT images. As the problem of low-quality soft tissue imaging with CBCT is almost nonexistent when imaging non-soft tissues, CBCT has been widely used in dentistry, where bone tissue is predominantly observed. [14] In contrast, the low quality of CBCT for imaging soft tissues hinders the identification of lesions [15] in medical specialties such as otorhinolaryngology. Consequently, the utility of CBCT has been limited in those specialties despite its advantages. In otorhinolaryngology, for instance, surgery is required for disease control of the sinonasal fungal ball because it is a frequent disease in the maxillary sinus that does not disappear spontaneously. Hence, simple CRS should be accurately distinguished from fungal balls in the early stage of the disease, and CT is essential for such diagnosis [16]. However, CBCT is rarely used because of its insensitivity to soft-tissue differentiation in the maxillary sinus. Reliably detecting lesions in soft tissues using CBCT remains challenging and requires assessment by experienced specialists who have observed and treated several patients with the same lesion type by comparing paired CBCT and MDCT images.

### **1.3 Artificial intelligence to overcome shortcomings of CBCT**

In recent years, numerous studies on artificial intelligence (AI)-based automatic lesion diagnosis in recent years have demonstrated high diagnostic performance comparable to that of an experienced physician [17] or diagnostic support to physicians by AI solutions. Accordingly, AI has been applied to CBCT, achieving high quality and useful automatic diagnosis [18, 19, 20, 21, 22]. AI-based processing can be viewed as automatically separating noise and disease information in a CBCT image to then identify the disease type by focusing on the corresponding information. As lesions and noise in CBCT images show distinctive patterns, AI-based computer-aided diagnosis (CAD) may help to identify a lesion using CBCT more accurately or effectively than a physician. Thus, AI-based CAD may effectively compensate for noise and artifacts in CBCT processing given the ability of AI to separate noise from the target lesion and provide more accurate diagnostic information to physicians than manual CBCT analysis.

Despite the technological aspirations, available AI-based CAD technology for CBCT has only been successfully applied to diseases related to the skeletal system, which can be imaged even by CBCT. However, no studies have achieved superior diagnosis of soft tissue lesions using CBCT, for which unmet demands in clinical fields beyond dentistry persist [19, 20, 21, 22]. Serindere et al. [18] evaluated the diagnostic performance of CBCT by applying AI-based CAD to maxillary sinusitis, a lesion that primarily affects soft tissues. Although they confirmed the superiority of AI-based CAD using CBCT in comparison with panoramic images, no absolute advantage or technical difference between AI-based CAD using CBCT and other imaging modalities has been verified.

### **1.4 Our contributions**

AI-based CAD using CBCT can reduce the inherent CBCT noise and then identify a disease or other health conditions in a noise-free environment. However, such an approach has not been devised, impeding the confirmation of its superiority and efficacy. Except for the aforementioned studies, to the best of our knowledge, AI solutions for CBCT have not been focused on diagnosis but instead included image restoration [23, 24, 25, 26, 27, 28, 29, 30] and segmentation [31, 32, 33, 34]. Overall, no study has demonstrated the clinical utility of the advancement of AI-based CAD methods using CBCT. Nevertheless, it seems possible to diagnose soft tissue lesions to outperform existing AI-based CAD using CBCT.

The contributions of this study to meet technical and clinical requirements for AI-based CAD using CBCT are summarized as follows:

- Unlike existing developments [35, 36, 37, 38], which perform CAD by merely applying existing AI technology to CBCT images, our AI-based CAD method using CBCT incorporates an AI-based denoising stage. Furthermore, existing denosing technique studies on CBCT [39, 40, 41] do not apply them to the diagnostic technology, whereas our study is the first for this application, demonstrating its technical distinctiveness and clinical superiority.
- We apply and evaluate the proposed method to discriminate fungal balls, sinusitis, and normal cases in the maxillary sinus. Fungal balls in the maxillary sinuses constitute a typical condition whose early diagnosis is crucial considering its bad prognosis, especially for the elderly [42]. Condition scanning using CBCT has attracted attention owing to the reduced radiation risk to the patient. However, existing methods for lesion localization on CBCT images in the presence of noise may be inaccurate, and physicians cannot rely on the CAD findings. In contrast, the proposed AI-based CAD system synthesizes a denoised full-dose reference MDCT image from the corresponding CBCT scan using an embedded denoising method to then accurately localize lesions. The proposed method may facilitate and increase the accuracy of diagnosis, supporting physicians in understanding automatic diagnosis data.
- We demonstrate that the proposed AI-based CAD method for CBCT achieves superior diagnostic performance than an existing method, with improvements in the micro-average area under the curve (AUC), macro-average AUC, and accuracy by 7.4, 5.6, and 9.6% (from 86.2, 87.0, and 73.4 to 93.6, 92.6, and 83.0%), respectively. In a comparative evaluation with assessments by six otorhinolaryngology resident physicians, the proposed method showed improved accuracy by 11.3% (from 71.7 to 83.0%), demonstrating its clinical value. For a fair evaluation, we used data from Samsung Seoul Medical Center for training (i.e., internal set) and Samsung Changwon Medical Center for evaluation (i.e., external set).
- We demonstrate that using medical imaging equipment capable of concurrently performing CBCT and MDCT image restoration has great prospective applications. For instance, training AI-based CAD based on pairs of collected CBCT and MDCT images may allow to subsequently perform efficient diagnosis solely using CBCT (with a low dose) while omitting both MDCT imaging and additional training. Our development and findings demonstrate the feasibility of this approach.

## 2 Methods

### 2.1 Data acquisition and preprocessing

#### 2.1.1 Data acquisition and annotation

**Table 1:** Number of 3D stacks for OMU R-MDCT per class in internal and external sets

Data type	Internal set ( $n$ )	External set ( $n$ )
HC	130	20
CRS	128	18
MFB	254	26
Total	512	64

Real MDCT (R-MDCT) data were collected to synthesize pseudo-CBCT (P-CBCT) data. R-MDCT data consisted of internal and external sets, which were collected from Samsung Seoul Medical Center (Seoul, Republic of Korea) and Samsung Changwon Medical Center (Changwon, Republic of Korea), respectively, after approval by the Institutional Review Board (approval number: 2020-07-173). At 120 kVP and 2 mm-thick

tubular surface slices, R-MDCT images from each institution were acquired using the same parameters. The R-MDCT internal set included 512 3D stacks of ostiomeatal unit (OMU) MDCT head images acquired once from 512 participants. The external set consisted of 64 3D stacks from 64 subjects. The internal data included 254 maxillary sinus fungal balls (MFB) [42], 128 chronic rhinosinusitis (CRS), and 130 healthy control (HC) cases as disease classes, while the external data included 26 MFB, 18 CRS, and 20 HC cases.

We requested annotations for the internal and external sets to ear, nose, and throat (ENT) physicians. Because each patient had a different disease status on the right or left side, each 3D OMU MDCT stack was divided into right and left halves, and each ENT physician was required to annotate either of the three disease classes on each side of the maxillary sinuses (i.e., HC, CRS, or MFB per side). Subsequently, individual annotations were confirmed by at least three experts for labeling after reaching a consensus. We obtained annotations from four ENT physicians with less than 10 years of experience and four specialists with more than 10 years of experience. In addition, for the AI-based CAD method to first distinguish slices corresponding to the maxillary sinuses before disease detection to constrain the disease area within the maxillary sinuses, we requested the ENT physicians to identify the entire (coronal view) slices in the R-MDCT samples showing the maxillary sinuses in both the internal and external sets.

### 2.1.2 Data preprocessing: P-CBCT synthesis from R-MDCT

As illustrated in Fig. 1, we obtained the 3D stack of P-CBCT from the individual 3D stack of OMU MDCT data. To this end, each 3D stack of OMU MDCT was assumed to show the patient’s head, and CBCT was reconstructed using the projection images produced by executing a cone-beam projection. The projector rotated 180 degrees around the cephalic (i.e., R-MDCT 3D stack) about the horizontal axis, taking one shot every 2 degrees to collect 90 projection images before reconstruction using the Feldkamp–Davis–Kress [43] method to obtain a 3D stack of P-CBCT. For consistency with the actual imaging setup, we set the source–object distance (i.e., the distance between the X-ray source and patient), object–image distance (i.e., the distance between the patient and detector), and detector size to 1200, 200, and 512 mm, respectively, using the ASTRA toolbox [44]. As an obtained P-CBCT image was reconstructed from an existing R-MDCT image, the P-CBCT images used the annotations of the R-MDCT described in Section 2.1.1. Finally, the number of synthesized P-CBCT images was the number of acquired 3D stacks of R-MDCT. The internal P-CBCT set ( $n = 512$ ) was used for training, and the external P-CBCT set ( $n = 64$ ) was used for diagnostic performance evaluation.

## 2.2 AI-based method for lesion diagnosis on OMU CBCT

We introduce an advanced AI-based CAD method intended for CBCT and compare it with our previous development [45] considered as the baseline in the present study. Sections 2.2.1 and 2.2.2 detail the diagnosis (inference) of the proposed method and its training processes, respectively, compared with those of the baseline.

### 2.2.1 Inference for CAD

The inference processes of the baseline and proposed AI-based CAD methods are illustrated in Figs. 2(a) and (b), respectively, and described below.

The baseline method receives a 3D OMU R-MDCT stack as input and generates a stack only containing the maxillary sinus region from a 2D convolutional neural network (CNN) [46] that extracts only the slices with visible maxillary sinuses among the coronal slices (first stage). The diagnosis is predicted using a 3D CNN [47] that performs individual disease diagnosis for each sinus region (second stage). Fig. 2(a) describes this two-stage diagnosis process, which allows to perform accurate AI-based CAD of diseases within the region of interest

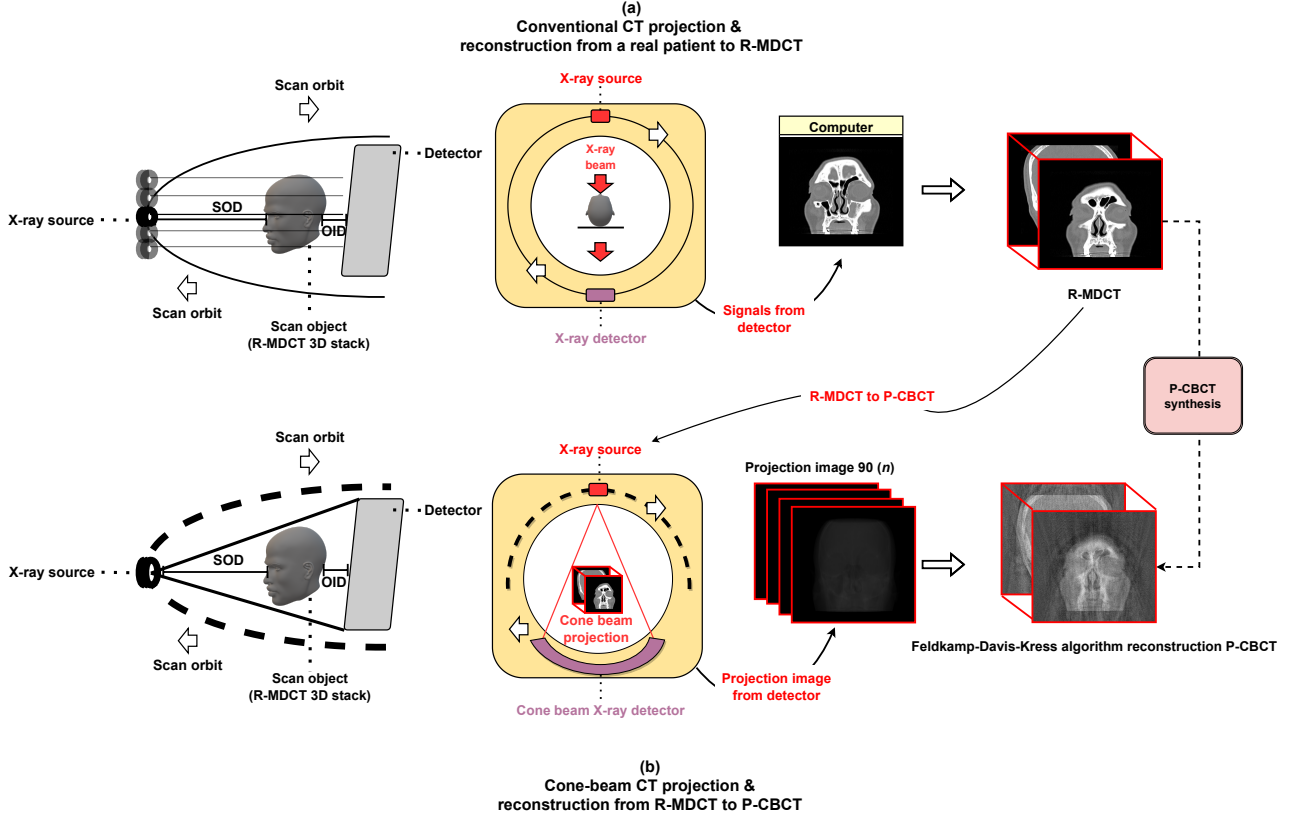


**Figure 1: P-CBCT image synthesized from R-MDCT scans based on 3D cone-beam projection and reconstruction.**

(a) Schematic for obtaining R-MDCT data (conventional MDCT projection and reconstruction from an actual patient to R-MDCT). (b) Schematic for obtaining P-CBCT data (cone-beam MDCT projection and conversion from R-MDCT into P-CBCT data). (OID, object–image distance; SOD, source–object distance)

(i.e., maxillary sinuses) in the original 3D OMU R-MDCT stack. The method achieves superior diagnostic performance to that of ENT resident physicians in a fully end-to-end approach, as the diagnosis can be done by directly using OMU MDCT images without any pretreatment assumptions. The baseline can achieve accurate diagnosis without noise and artifacts, like in MDCT data, but it shows technical limitations for CBCT data that are generally polluted by strong noise and artifacts. For example, in some instances, the baseline shows poor diagnostic performance of lesions in some instances. In addition, the lesions are not apparent owing to CBCT noise, hindering the confirmation of diagnosis by a physician even when examining the region of interest on the CBCT image with the baseline results, indicating limited interpretive power.

To improve the diagnostic performance and interpretive power, we incorporate denoising before diagnosis, establishing a novel AI-based CAD method that merges the two diagnosis stages preceded by the additional denoising stage for accurate diagnosis. The proposed method thus comprises the novel denoising (first stage) and the baseline stages of extracting the maxillary sinus region (second stage) and performing disease diagnosis in each maxillary sinus region (third stage). The processes of the proposed method are illustrated in Fig. 2(b).

The proposed AI-based CAD method eliminates noise and artifacts from CBCT images, as illustrated in the



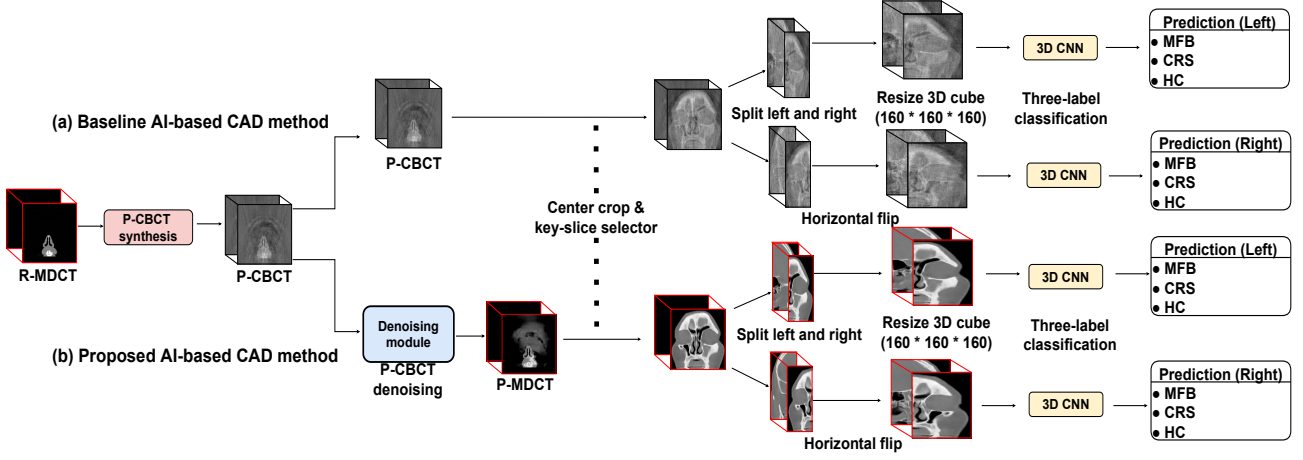


**Figure 2: Inference of (a) baseline and (b) proposed AI-based CAD methods.** The proposed method takes a 3D stack of OMU CBCT scans from a target subject as input. Unlike the baseline method, denoising is performed using a specific module (block in blue). A denoised 3D stack is derived as pseudo-MDCT. Using the 3D pseudo-MDCT stack, diagnosis is performed as in the baseline method [45]: extraction of the maxillary sinus region and diagnosis of diseases within that area through three-label classification.

first stage of Fig. 2(b). Thus, it allows the synthesis of realistic pseudo-MDCT (P-MDCT) images. The P-MDCT images with mitigated noise promote disease identification by both a CAD method and a physician responsible for confirming the diagnosis. Therefore, the diagnostic performance of AI-based CAD and the physician’s ability to interpret the results can be enhanced. This study is a pioneering demonstration of the importance of noise removal as an initial stage for AI-based CAD using CBCT, as verified by comparisons with results without denoising.

### 2.2.2 Training

We describe and compare the training processes of the proposed and baseline AI-based CAD methods. The processes are illustrated in Fig. 3. Unlike the baseline, the proposed method includes training for denoising, while the remainder is the same as baseline training.

**Denoising module.** To train the denoising module in the proposed method, we define a reconstruction loss such that the module output is an estimate of the 3D R-MDCT stack, called the 3D stack of pseudo-MDCT (P-MDCT), which represents the same data as the denoising module input, that is, the 3D P-CBCT stack. In other words, we generate the P-CBCT image from the R-MDCT image as described in Section 2.1.2 and then use the P-CBCT image as input of the denoising module to be trained aiming to obtain the original R-MDCT as its output. Training of the denoising module proceeds as follows:

- The denoising module is trained using multiscale U-Net-like sparse coding (MUSC) [48], which demonstrated the best performance compared with other denoising modules evaluated in this study. Nevertheless, other more advanced denoising models may be implemented in the future for the proposed method. Paired R-MDCT and P-CBCT images are used as training data because MUSC requires supervised learning. Training is performed in a 2D slice-by-slice process using the corresponding slices in each cube of R-MDCT and P-CBCT scans.

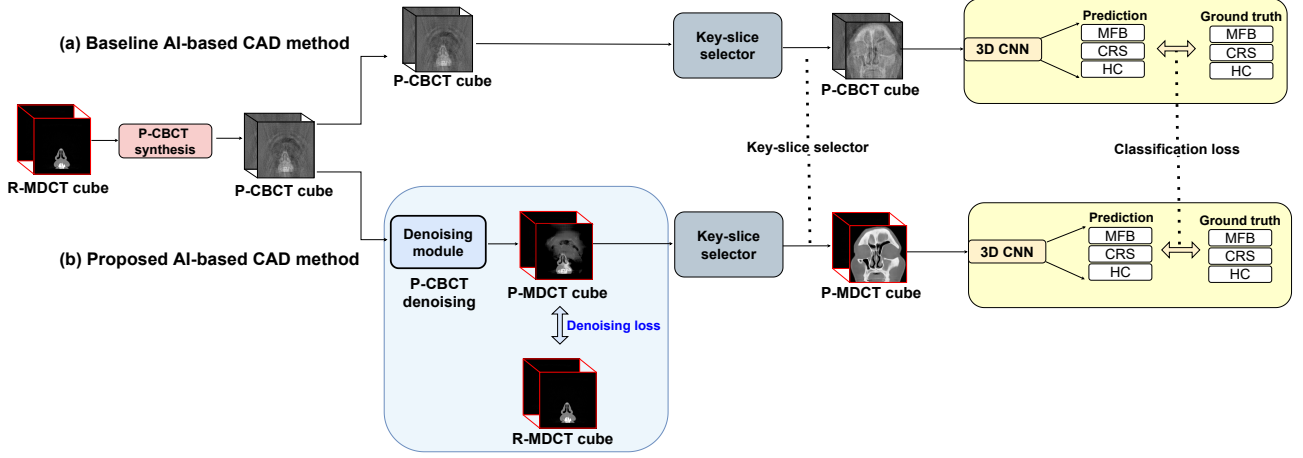


**Figure 3: Training processes of (a) baseline and (b) proposed AI-based CAD methods.** Unlike the baseline, the proposed method includes a denoising module adding a denoising loss to the output. Both methods use a classification loss in the last stage for diagnosis.

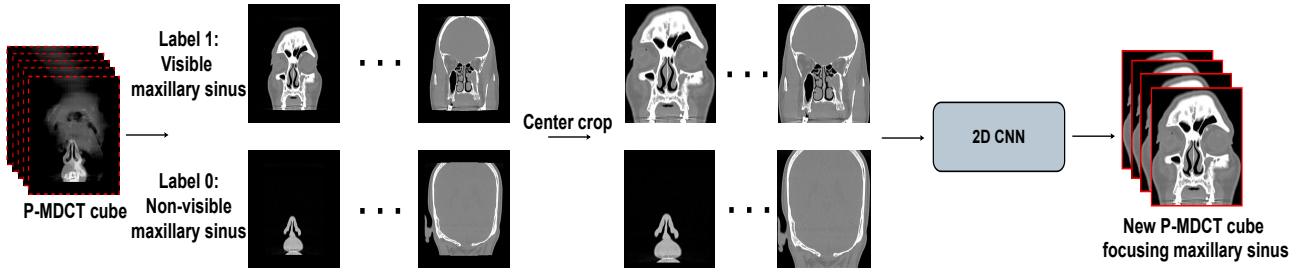


**Figure 4: Process of key-slice selector.** This network extracts slices only including maxillary sinuses and generates the corresponding 3D P-MDCT stack.

- We use the mean squared error in the denoising module as a representative reconstruction loss to generate P-MDCT from P-CBCT images. The denoising module accepts as input individual coronal 2D slices of each 3D stack resized to slices of  $512 \times 512$  pixels and outputs same-sized slices. Training is conducted with a batch size of 18, a learning rate of  $10^{-4}$ , 20 epochs, and Adam optimization [49]. We used the internal set with 512 3D stacks for training, and the external set for testing the trained denoising module.

**Diagnosis module.** In the proposed method, the diagnosis module takes the noise-removed 3D stack from the denoising module as input and identifies the disease type (i.e., MFB, CRS, or HC) of the left and right maxillary sinuses. To predict the confirmed label provided by the physician (see Section 2.1.1) as the output of the diagnosis module, we assign a classification loss to the module output. The diagnosis module has a similar baseline to the proposed technique, but it receives the 3D CBCT stack as input, whereas the proposed technique receives the denoising output of this stack. Details of the diagnosis module can be found in our previous report [45]. The module consists of a key-slice selector followed by a multilabel classifier summarized as follows:

- Key-slice selector. The key-slice selector uses a 3D stack of head scans (i.e., 3D P-MDCT stack in the proposed method or 3D CBCT stack in the baseline method) from a patient as input. Only the coronal slices with the visible regions of maxillary sinuses are extracted to build the corresponding 3D stack. To



this end, each coronal slice is used for training the key-slice selector to perform binary classification of the maxillary sinus presence. As a representative backbone network, we use Efficient-Net [50], which achieved the highest performance in our previous study [45]. Using the common classification loss given by cross-entropy [51], the model is trained to deliver label 1 if the maxillary sinus is visible and label 0 otherwise. The ground truth label is that provided by the physician. Fig. 4 illustrates key-slice selection, and additional training details are available in our previous study [45].

- **Multilabel classifier.** We use a 3D stack centered on the maxillary sinuses obtained from the key-slice selector as input for the classification of another network, which predicts one of three labels for diagnosing the disease type in the left and right maxillary sinuses. As the delicate correlation between slices is important for the differentiation and detection of MFS and CRS, we use a 3D CNN instead of a 2D architecture, which was used in our previous study [45]. We divide the original 3D cube, including only the maxillary sinuses into two 3D cubes for the right and left sides, such that each maxillary sinus is centered, and the network receives the divided 3D cube as input for learning based on the cross-entropy loss to predict the disease type among MFB, CRS, and HC. We use 3D-ResNet [52] as the backbone of the 3D CNN using the weights from pretraining on the Kinetics dataset [53]. Additional training details are available in our previous study [45].

The training was conducted using fivefold cross-validation and the internal set, and model evaluation was then performed on the external set.

### 2.3 Evaluation metrics

The following five statistical metrics were used to evaluate the performance of the classification model: accuracy, AUC of the receiver operating characteristic curve, sensitivity, precision, and F1 score. As the classification of three labels was performed, we used three groups for true positive (TP), false positive (FP), and false negative (FN) results with labels 1, 2, and 3 for MFB, CRS, and HC, respectively. One label was selected as positive and the other two as negative.

$$Accuracy = \frac{\sum_{i=1}^C T_i}{D_{test}} \quad (1)$$

$$Precision = \frac{1}{C} \sum_{i=1}^C Precision_i = \frac{1}{C} \sum_{i=1}^C \frac{TP_i}{TP_i + FN_i} \quad (2)$$

$$Sensitivity = \frac{1}{C} \sum_{i=1}^C Sensitivity_i = \frac{1}{C} \sum_{i=1}^C \frac{TP_i}{TP_i + FN_i} \quad (3)$$

$$F1\_score = \frac{1}{C} \sum_{i=1}^C F1\_score_i = \frac{2}{C} \sum_{i=1}^C \frac{Precision_i \cdot Sensitivity_i}{Precision_i + Sensitivity_i} \quad (4)$$

where  $C$  ( $= 3$ ) is the number of labels to be classified and  $T_i$  is the number of correctly predicted samples for label  $i$ . Considering label  $i$  as positive and the remaining labels as negative,  $TP_i$ ,  $FP_i$ , and  $FN_i$  represent the true positive, false positive, and false negative, respectively, and  $Precision_i$ ,  $Sensitivity_i$ , and  $F1\_score_i$  represent the precision, sensitivity, and F1 score for label  $i$ , respectively.

### 3 Results

#### 3.1 Quantitative evaluation

We quantitatively compared the baseline and proposed AI-based CAD methods to determine whether the performance was enhanced by adding a denoising module. In addition, we compared the proposed CAD with the physician’s diagnoses to evaluate the clinical usefulness of our proposal. These comparisons are respectively reported in Sections 3.1.1 and 3.1.2.

##### 3.1.1 Diagnostic performance of baseline and proposed methods

**Table 2: Diagnostic performance of baseline and proposed AI-based CAD methods.** Micro- and macro-average AUCs obtained from external validation. Mean and standard deviation derived from fivefold cross-validation.

Metric	External validation result (%)
Micro-average AUC (Baseline)	$86.2 \pm 8.8$
Macro-average AUC (Baseline)	$87.0 \pm 4.1$
Accuracy (Baseline)	$73.4 \pm 9.34$
Micro-average AUC (Proposed)	<b><math>93.6 \pm 1.7 (+7.4)</math></b>
Macro-average AUC (Proposed)	<b><math>92.6 \pm 2.3 (+5.6)</math></b>
Accuracy (Proposed)	<b><math>83.0 \pm 2.0 (+9.6)</math></b>

**Table 3: Diagnostic performance of baseline and proposed AI-based CAD methods.** Accuracy, sensitivity, precision, and F1 score obtained from external validation. Mean and standard deviation derived from fivefold cross-validation.

Method	Accuracy (%)			
Baseline	$73.4 \pm 10.4$			
Proposed	<b><math>83.0 \pm 2.3 (9.6) \uparrow</math></b>			
Method	Sensitivity (%)			
	HC	CRS	MFB	Average
Baseline	$83.0 \pm 20.8$	$35.0 \pm 19.0$	$69.3 \pm 21.8$	$62.4 \pm 4.0$
Proposed	$90.6 \pm 3.4$	$69.5 \pm 13.3$	$77.4 \pm 0.4$	<b><math>79.2 \pm 3.6 (16.8) \uparrow</math></b>
	Precision (%)			
Baseline	$91.9 \pm 4.1$	$30.5 \pm 20.2$	$73.2 \pm 15.9$	$65.2 \pm 8.4$
Proposed	$93.7 \pm 4.7$	$66.7 \pm 5.8$	$75.6 \pm 6.6$	<b><math>78.7 \pm 2.8 (13.5) \uparrow</math></b>
	F1 score (%)			
Baseline	$85.8 \pm 12.9$	$28.0 \pm 6.9$	$67.4 \pm 12.6$	$60.4 \pm 7.3$
Proposed	$92.0 \pm 1.7$	$67.3 \pm 6.8$	$76.4 \pm 3.1$	<b><math>78.6 \pm 3.1 (18.2) \uparrow</math></b>

**Performance of baseline and proposed AI-based CAD methods.** The diagnostic performance results of the baseline and proposed AI-based CAD methods are listed in Tables 2 and 3 regarding AUC and other metrics. As shown in Fig. 2, the two methods use a 3D P-CBCT stack input and provide individual diagnostic outcomes for each sinus. We converted all the 3D R-MDCT stacks in the external stack into 3D P-CBCT stacks and used them as inputs. The average performance across sinuses was calculated for each of the five trained/cross-validation models, and their averages and standard deviations are also listed in the tables.

In Table 2, the proposed method increases the micro- and macro-average AUCs by 7.4% and 5.6%, respectively, compared with the baseline. In Table 3, the proposed method enhances the performance by at least 10%

**Table 4: Noise cancellation performance using different denoising models in the proposed technique.** PSNR [58] and SSIM [59] were evaluated.

Model	PSNR (dB)	SSIM (%)
GAN-based		
Cycle-GAN [54]	$12 \pm 0.9$	$53 \pm 5.3$
DCL-GAN [55]	$17 \pm 1.5$	$58 \pm 5.7$
U-Net-based		
U-Net [56]	$20 \pm 2.2$	$81 \pm 5.0$
CNCL-U-Net-denoising [57]	$19 \pm 3.3$	$83 \pm 6.6$
MUSC [48]	<b><math>20 \pm 1.2</math></b>	<b><math>83 \pm 4.8</math></b>

compared with the baseline for all the metrics of accuracy, specificity, sensitivity, and F1 score. These results verify the efficacy of the proposed method that adds the denoising module.

**Performance of different denoising models in the proposed method.** To evaluate the backbone of the denoising module in the proposed method, we compared four backbone models: Cycle-GAN [54], DCL-GAN [55], U-Net [56], CNCL-U-Net-denoising [57], and MUSC [48]. In this evaluation, only annotated coronal 2D slices (paired R-MDCT and P-CBCT images) of the maxillary sinus were collected from the internal set. From the slices, 1000 were randomly selected and used for evaluation, and the rest were used for training. The two generative adversarial networks (GANs) are high-performance models in image translation that we used to convert a noisy image into a denoised image. We used the original GAN code and the associated loss in the evaluation. U-Net was trained as described in Section 2.2.2. Table 4 shows the denoising performance results (i.e., peak signal-to-noise ratio (PSNR) and structural similarity index (SSIM)) for each different model. The U-Net-based model showed higher performance than the GAN-based model, and MUSC showed the highest performance, which therefore was used in this study as a representative denoising model.

### 3.1.2 Diagnostic performance of proposed method and physician

**Table 5: Diagnostic performance of proposed AI-based CAD method and otorhinolaryngology resident physicians.** Micro- and macro-average AUCs obtained from external validation. Mean and standard deviation derived from fivefold cross-validation.

Method	Average accuracy (%)			
Manual	$71.7 \pm 2.8$			
Proposed	<b><math>83.0 \pm 2.3</math></b> (11.3) $\uparrow$			
Method	Sensitivity (%)			
	HC	CRS	MFB	Average
Manual	$95.9 \pm 0.6$	$52.5 \pm 14.8$	$32.5 \pm 9.9$	$60.3 \pm 3.4$
Proposed	$90.6 \pm 3.4$	$69.5 \pm 13.3$	$77.4 \pm 0.4$	<b><math>79.2 \pm 3.6</math></b> (18.9) $\uparrow$
Precision (%)				
Manual	$94.3 \pm 0.0$	$46.8 \pm 5.0$	$40.0 \pm 8.8$	$60.4 \pm 4.3$
Proposed	$93.7 \pm 4.7$	$66.7 \pm 5.8$	$75.6 \pm 6.6$	<b><math>78.7 \pm 2.8</math></b> (18.3) $\uparrow$
F1 score (%)				
Manual	$95.1 \pm 0.3$	$49.1 \pm 9.1$	$35.0 \pm 7.2$	$59.7 \pm 3.1$
Proposed	$92.0 \pm 1.7$	$67.3 \pm 6.8$	$76.4 \pm 3.1$	<b><math>78.6 \pm 3.1</math></b> (18.9) $\uparrow$

In addition to the comparative evaluation between the baseline and proposed methods, we compared the

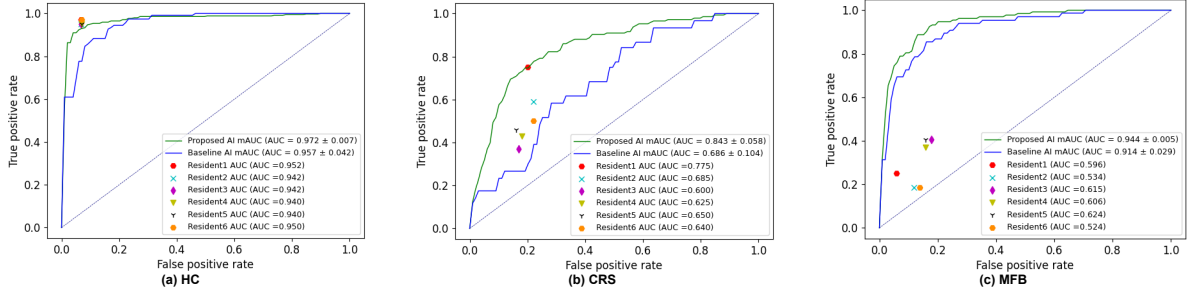


**Figure 5: Diagnostic performance of proposed AI-based CAD method and six resident physicians regarding the receiver operating characteristic curve for each disease type.** The proposed method provides average AUCs (mAUCs) for (a) HC, (b) CRS, and (c) MFB of  $0.972 \pm 0.007$  (95% confidence interval, 0.958 – 0.986),  $0.843 \pm 0.058$  (95% confidence interval, 0.729 – 0.957), and  $0.944 \pm 0.005$  (95% confidence interval, 0.934 – 0.954), respectively.

results from our proposal and external validation by six otolaryngology resident physicians to evaluate the clinical superiority of the proposed AI-based CAD method. The resident physicians who participated in this test were not involved in data extraction and annotation. In other words, the six physicians and the proposed method performed ternary classification of the disease type for each sinus across all 3D P-CBCT stacks in the external validation set.

Table 5 lists this evaluation’s accuracy, specificity, and sensitivity results. The proposed method shows higher diagnostic performance for the three metrics than physicians by at least 10%. In particular, it substantially improves the sensitivity and specificity by at least 18%, demonstrating its clinical effectiveness.

In addition, the AUC was evaluated and compared for each disease class, obtaining the results shown in Fig. 5. The proposed method demonstrates comparable sensitivity/specificity in the normal group to the physicians and superior sensitivity/specificity for disease detection. In particular, for CRS detection, the baseline achieves a lower detection than a resident physician. In contrast, the proposed method has an average detection rate of at least 15% higher than that of the resident physician. These results confirm that the proposed method can outperform both human diagnosis and the existing CAD method.

## 3.2 Qualitative evaluation

We also performed qualitative comparisons for various coronal scans.

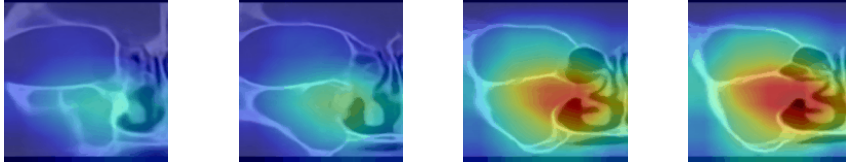
### 3.2.1 Gradient-weighted class activation maps of baseline and proposed methods

Fig. 6 shows activation maps obtained from the baseline and proposed AI-based CAD methods. The maps show relevant parts of the image for AI-based diagnosis obtained by gradient-weighted class activation mapping, as in our previous study [45]. The proposed method correctly detects diseased maxillary sinuses, as highlighted in the maps, and correctly classifies the disease type (i.e., CRS or MFB). On the other hand, the baseline method fails to detect the maxillary sinus and classify the disease.

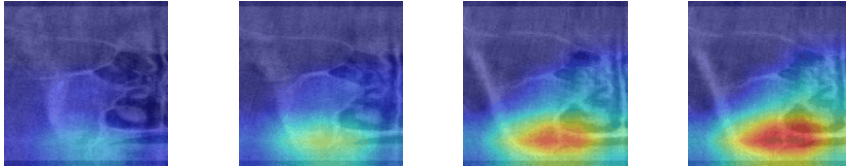
Unlike the baseline, the proposed method provides denoised scans (P-MDCT images) as input CBCT scans. Fig. 6 shows that the proposed method uses denoised scans as background in each activation map, whereas the baseline method should rely on the original CBCT scan as background. Hence, the activation maps obtained from the proposed method show areas with apparent diseases on the denoised image. When a physician makes a final diagnosis by referring to the CAD results, the proposed method allows the examination of denoised scan

findings in highly active map areas, thus facilitating the CAD interpretation by the physician. In contrast, the baseline method provides activation maps considering raw CBCT scans that inevitably contain noise and artifacts. As noise and distortions pollute the activation map, the physician cannot easily assess the result accuracy and interpret the diagnosis.

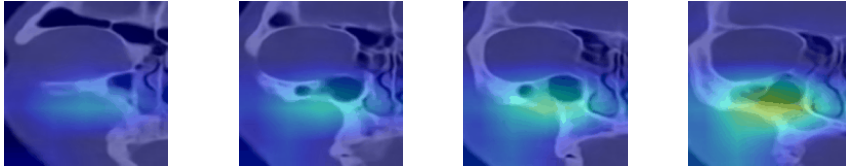
**(a) Proposed method validation with MFB patient (Actual: MFB, Predict: MFB)**



**(b) Baseline method validation with MFB patient (Actual: MFB, Predict: CRS)**



**(c) Proposed method validation with CRS patient (Actual: CRS, Predict: CRS)**



**(d) Baseline method validation with CRS patient (Actual: CRS, Predict: HC)**

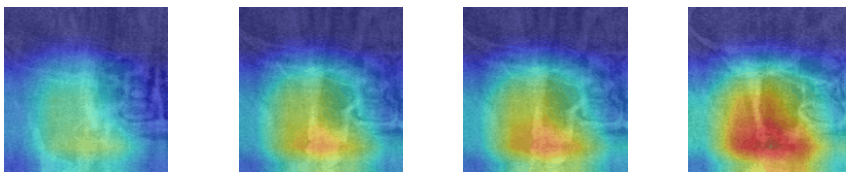


**Figure 6: Activation maps of diagnoses obtained from baseline and proposed methods.** Activation maps for (a,c) proposed and (b,d) baseline methods.

### 3.2.2 P-MDCT image estimated by denoising R-CBCT image

The proposed AI-based CAD method improves the diagnostic performance on CBCT scans compared with the baseline method and manual assessment. Hence, P-MDCT image estimation from a P-CBCT scan is validated. Nevertheless, the P-MDCT estimate from the denoising module in the proposed method is inferred from a P-CBCT image (i.e., CBCT scans are synthesized from MDCT scans). To evaluate this process, we tested noise removal of the trained denoising module in the proposed method for R-CBCT images in addition to P-CBCT

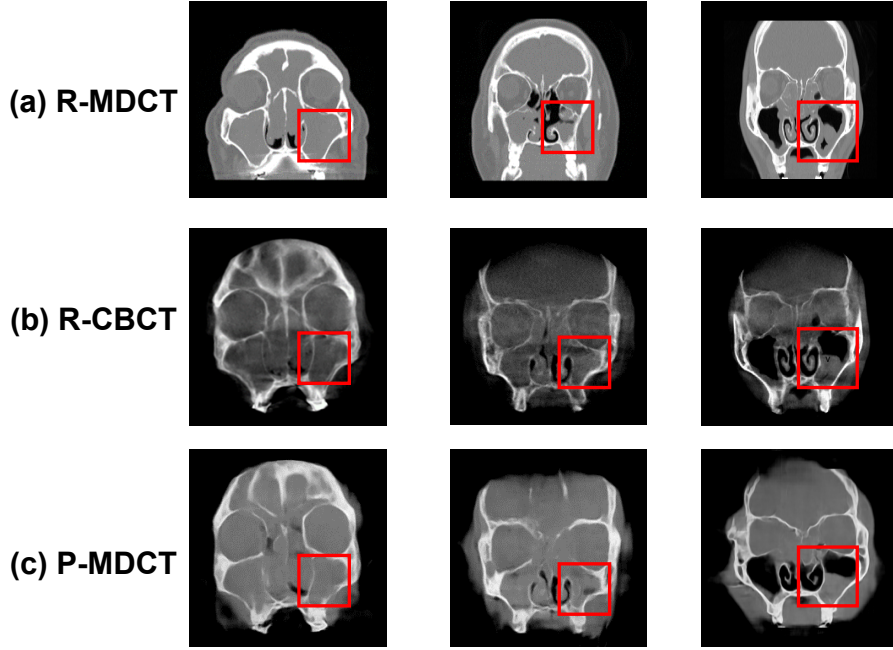


**Figure 7: Denoising examples of R-CBCT images.** (a) R-MDCT, (b) R-CBCT, and (c) P-MDCT (denoised R-CBCT) images.

images.

For this evaluation, physicians at our institution acquired three sets of patient-matched 3D stacks of R-MDCT and R-CBCT. The denoising module used the training weights obtained for diagnosis evaluation (see Section 3.2). Thus, R-CBCT data were not used for training the denoising module. Figs. 7(a)–(c) show R-MDCT, R-CBCT, and denoised R-CBCT images (denoted as P-MDCT images because they are the output of the trained denoising module), respectively. In P-MDCT images, noise in R-CBCT images is removed, and the same anomaly structure of the R-MDCT images is observed (red boxes). Thus, the denoising module can take an R-CBCT image as input and perform denoising to determine the corresponding P-MDCT image with no substantial disease-related artifacts. Consequently, P-MDCT images can be obtained not only using P-CBCT images but also R-CBCT images, demonstrating the wide applicability of the denoising module.

## 4 Discussion

**Clinical implications.** This study is the first to improve the discrimination of soft tissues, which is difficult in CBCT, through an AI-based method and improve CAD of lesions in the maxillary sinus, providing great clinical significance. As the demand for accurate diagnosis of CRS increases, the number of MDCT examinations is also increasing. However, CBCT is a more convenient alternative that uses less radiation at the expense of lower resolution around soft tissues and signal-to-noise ratio than MDCT. In addition, a fungal ball in the maxillary sinus is a disease that does not respond to drug treatments, including antibiotics, and thus requires surgery [60]. Therefore, early diagnosis is essential but often delayed given the difficulty of accurate diagnosis in CBCT images [61]. The proposed AI-based CAD method may be implemented in CBCT equipment and possibly support clinicians in the accurate identification of diseases that require surgery in the early stages.



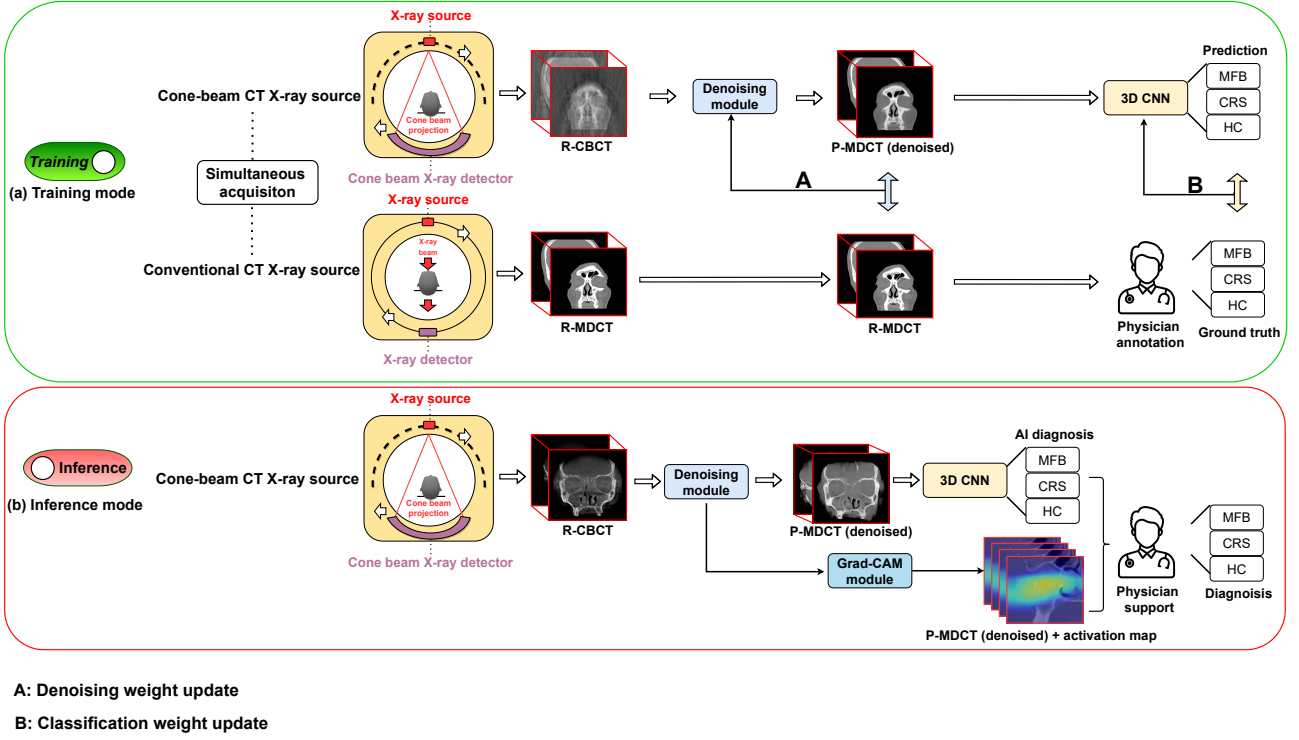


**Figure 8: New approach for radiographic image reconstruction using proposed AI-based CAD method.** (a) Simultaneous imaging of CBCT and MDCT for training diagnosis method. (b) Simultaneous acquisition of virtual MDCT and diagnoses from trained model using only CBCT image as input. (Grad-CAM, gradient-weighted class activation mapping)

**Technical implications.** This study has demonstrated the feasibility of using CBCT to detect maxillary sinus diseases by mitigating image noise, increasing the accuracy by 11.3% and 9.6% compared with manual assessment and a baseline method, respectively. Nevertheless, as the experimental evaluation only considered P-CBCT data (i.e., CBCT images synthesized from R-MDCT data) and not R-CBCT data, its validation with actual clinical data remains to be conducted.

Despite current limitations, we provide a new approach for developing CAD in medical devices, as illustrated in Fig. 8. If radiology medical equipment can acquire paired R-CBCT and R-MDCT scans, P-CBCT data used in this study can be substituted with R-CBCT data. Hence, if the proposed AI-based CAD method is applied to such a medical device, the denoising module can be trained to synthesize R-MDCT images from R-CBCT scans, and the subsequent diagnosis module can be trained to infer the corresponding diagnosis using the R-MDCT estimate as input. Therefore, a device capable of simultaneous CBCT and MDCT enables training of the CAD method using R-CBCT data (and its corresponding R-MDCT data) instead of P-CBCT data. The trained model performs diagnosis directly using R-CBCT images instead of R-MDCT images, allowing diagnosis at a low radiation dose.

In its current form, the proposed method provides not only a diagnosis result but also a denoised P-MDCT image and activation map from an R-CBCT image. Thus, practitioners can receive valuable assistance for interpreting AI CAD even from a CBCT scan. The benefits of the proposed method may justify the corresponding modification of medical device usage.

## 5 Conclusion

We demonstrate that eliminating noise from CBCT images can enhance the performance of AI-based CAD with a model-agnostic method. The proposed method justifies and validates the inclusion of noise removal for diagnosis in soft tissues using CBCT. Our results suggest a successful diagnosis of soft tissue lesions of the sinonasal area, outperforming a baseline method and specialists. We expect that the method will enable accurate diagnosis using only low-dose CBCT, thereby reducing the burden of examination for both clinicians and patients, particularly in locations with shortages of physicians and high-dose screening systems.

## Acknowledgements

This work was supported by a grant from the National Research Foundation of Korea (NRF) funded by the Korean government (MSIT) (2021R1F1A106153511), by a grant from Korea Medical Device Development Fund funded by the Korean government (Ministry of Science and ICT, Ministry of Trade, Industry and Energy, Ministry of Health & Welfare, Ministry of Food and Drug Safety) (202011B08-02, KMDF\_PR\_20200901\_0014-2021-02, RS-2020-KD000014), by the Technology Innovation Program (20014111) funded by the Ministry of Trade, Industry & Energy (MOTIE, Korea), and by the Future Medicine 20\*30 Project of Samsung Medical Center (SMX1210791).

## Data availability

The authors declare that the main data supporting the results of this study are available within the paper. The raw datasets are not widely available due to patient confidentiality and hospital privacy policy. The authors have no right to provide material to another person or institution.

## Code availability

The code used for the DL models is available on GitHub (To be disclosed upon submission of the revised version): [CBCT-DENOISING-CAD](#).

## References

- [1] Michael S Benninger, Berrylin J Ferguson, James A Hadley, Daniel L Hamilos, Michael Jacobs, David W Kennedy, Donald C Lanza, Bradley F Marple, J David Osguthorpe, James A Stankiewicz, et al. Adult chronic rhinosinusitis: Definitions, diagnosis, epidemiology, and pathophysiology. *Otolaryngology-Head and Neck Surgery*, 129(3):S1–S32, 2003.
- [2] Lisa Caulley, Kednapa Thavorn, Luke Rudmik, Chris Cameron, and Shaun J Kilty. Direct costs of adult chronic rhinosinusitis by using 4 methods of estimation: Results of the US medical expenditure panel survey. *Journal of Allergy and Clinical Immunology*, 136(6):1517–1522, 2015.
- [3] Emma C Cashman, Peter J MacMahon, and David Smyth. Computed tomography scans of paranasal sinuses before functional endoscopic sinus surgery. *World journal of radiology*, 3(8):199, 2011.
- [4] Sotirios Bisdas, Marjike Verink, Hartmut Peter Burmeister, Martin Stieve, and Hartmut Becker. Three-dimensional visualization of the nasal cavity and paranasal sinuses: Clinical results of a standardized approach using multislice helical computed tomography. *Journal of computer assisted tomography*, 28(5): 661–669, 2004.
- [5] Jeffrey M Albert. Radiation risk from CT: Implications for cancer screening. *American Journal of Roentgenology*, 201(1):W81–W87, 2013.
- [6] Jens De Cock, Federica Zanca, John Canning, Ruben Pauwels, and Robert Hermans. A comparative study for image quality and radiation dose of a cone beam computed tomography scanner and a multislice computed tomography scanner for paranasal sinus imaging. *European radiology*, 25(7):1891–1900, 2015.
- [7] Sua Yoo and Fang-Fang Yin. Dosimetric feasibility of cone-beam CT-based treatment planning compared to CT-based treatment planning. *International Journal of Radiation Oncology\* Biology\* Physics*, 66(5): 1553–1561, 2006.
- [8] Allan G Farman and William C Scarfe. The basics of maxillofacial cone beam computed tomography. *Seminars in Orthodontics*, 15(1):2–13, 2009.
- [9] Scott R Makins. Artifacts interfering with interpretation of cone beam computed tomography images. *Dental Clinics*, 58(3):485–495, 2014.
- [10] Lee A Feldkamp, Lloyd C Davis, and James W Kress. Practical cone-beam algorithm. *Josa a*, 1(6): 612–619, 1984.
- [11] Munetaka Naitoh, Kiyonobu Saburi, Kenichi Gotoh, Kenichi Kurita, and Eiichiro Arij. Metal artifacts from posterior mandibular implants as seen in CBCT. *Implant dentistry*, 22(2):151–154, 2013.
- [12] Richard A Zoumalan, Richard A Lebowitz, Edwin Wang, Kathryn Yung, James S Babb, and Joseph B Jacobs. Flat panel cone beam computed tomography of the sinuses. *Otolaryngology—Head and Neck Surgery*, 140(6):841–844, 2009.
- [13] Pallavi Agrawal, Sheetal Sanikop, and Suvarna Patil. New developments in tools for periodontal diagnosis. *International dental journal*, 62(2):57–64, 2012.
- [14] Hadi Mohammed Alamri, Mitra Sadrameli, Mazen Abdullah Alshalhoob, and MA Alshehri. Applications of CBCT in dental practice: a review of the literature. *General dentistry*, 60(5):390–400, 2012.

- [15] Rhita C Almeida, Lucia HS Cevdanes, Felipe AR Carvalho, Alexandre T Motta, Marco AO Almeida, Martin Styner, Timothy Turvey, William R Proffit, and Ceib Phillips. Soft tissue response to mandibular advancement using 3D CBCT scanning. *International journal of oral and maxillofacial surgery*, 40(4): 353–359, 2011.
- [16] Fabio Pagella, Elina Matti, Francesca De Bernardi, Lucia Semino, Caterina Cavanna, Piero Marone, Claudio Farina, and Paolo Castelnovo. Paranasal sinus fungus ball: Diagnosis and management. *Mycoses*, 50(6):451–456, 2007.
- [17] Abhimanyu S Ahuja. The impact of artificial intelligence in medicine on the future role of the physician. *PeerJ*, 7:e7702, 2019.
- [18] Gozde Serindere, Ersen Bilgili, Cagri Yesil, and Neslihan Ozveren. Evaluation of maxillary sinusitis from panoramic radiographs and cone-beam computed tomographic images using a convolutional neural network. *Imaging Science in Dentistry*, 52, 2022.
- [19] Teruhiko Hiraiwa, Yoshiko Ariji, Motoki Fukuda, Yoshitaka Kise, Kazuhiko Nakata, Akitoshi Katsumata, Hiroshi Fujita, and Eiichiro Ariji. A deep-learning artificial intelligence system for assessment of root morphology of the mandibular first molar on panoramic radiography. *Dentomaxillofacial Radiology*, 48(3): 20180218, 2019.
- [20] Frank C Setzer, Katherine J Shi, Zhiyang Zhang, Hao Yan, Hyunsoo Yoon, Mel Mupparapu, and Jing Li. Artificial intelligence for the computer-aided detection of periapical lesions in cone-beam computed tomographic images. *Journal of endodontics*, 46(7):987–993, 2020.
- [21] Romina Brignardello-Petersen. Artificial intelligence system seems to be able to detect a high proportion of periapical lesions in cone-beam computed tomographic images. *The Journal of the American Dental Association*, 151(9):e83, 2020.
- [22] Sujin Yang, Hagyeong Lee, Byoungchan Jang, Kee-Deog Kim, Jaeyeon Kim, Hwiyoung Kim, and Wonse Park. Development and validation of a visually explainable deep learning model for classification of C-shaped canals of the mandibular second molars in periapical and panoramic dental radiographs. *Journal of Endodontics*, 2022.
- [23] Jae Joon Hwang, Yun-Hoa Jung, Bong-Hae Cho, and Min-Suk Heo. Very deep super-resolution for efficient cone-beam computed tomographic image restoration. *Imaging Science in Dentistry*, 50(4):331, 2020.
- [24] Tobias Würfl, Mathis Hoffmann, Vincent Christlein, Katharina Breininger, Yixin Huang, Mathias Unberath, and Andreas K Maier. Deep learning computed tomography: Learning projection-domain weights from image domain in limited angle problems. *IEEE transactions on medical imaging*, 37(6):1454–1463, 2018.
- [25] Elias Eulig, Joscha Maier, Michael Knaup, N Robert Bennett, Klaus Hörndler, Adam S Wang, and Marc Kachelrieß. Deep learning-based reconstruction of interventional tools and devices from four X-ray projections for tomographic interventional guidance. *Medical physics*, 48(10):5837–5850, 2021.
- [26] Liyue Shen, Wei Zhao, Dante Capaldi, John Pauly, and Lei Xing. A geometry-informed deep learning framework for ultra-sparse 3D tomographic image reconstruction. *Computers in Biology and Medicine*, page 105710, 2022.

- [27] Mareike Thies, Jan-Nico Zäch, Cong Gao, Russell Taylor, Nassir Navab, Andreas Maier, and Mathias Unberath. A learning-based method for online adjustment of C-arm cone-beam CT source trajectories for artifact avoidance. *International journal of computer assisted radiology and surgery*, 15(11):1787–1796, 2020.
- [28] Liyue Shen, Wei Zhao, and Lei Xing. Patient-specific reconstruction of volumetric computed tomography images from a single projection view via deep learning. *Nature biomedical engineering*, 3(11):880–888, 2019.
- [29] Andreas Hauptmann, Jonas Adler, Simon Arridge, and Ozan Öktem. Multi-scale learned iterative reconstruction. *IEEE transactions on computational imaging*, 6:843–856, 2020.
- [30] Ye Liang, JingJing Huan, Jia-Da Li, CanHua Jiang, ChangYun Fang, and YongGang Liu. Use of artificial intelligence to recover mandibular morphology after disease. *Scientific reports*, 10(1):1–11, 2020.
- [31] Pierre Lahoud, Mostafa EzEldeen, Thomas Beznik, Holger Willems, André Leite, Adriaan Van Gerven, and Reinhilde Jacobs. Artificial intelligence for fast and accurate 3-dimensional tooth segmentation on cone-beam computed tomography. *Journal of Endodontics*, 47(5):827–835, 2021.
- [32] Xiang Lin, Yujie Fu, Genqiang Ren, Xiaoyu Yang, Wei Duan, Yufei Chen, and Qi Zhang. Micro-computed tomography-guided artificial intelligence for pulp cavity and tooth segmentation on cone-beam computed tomography. *Journal of Endodontics*, 47(12):1933–1941, 2021.
- [33] Adithya A Sherwood, Anand I Sherwood, Frank C Setzer, Jasmin V Shamili, Caroline John, Falk Schwen-dicke, et al. A deep learning approach to segment and classify C-shaped canal morphologies in mandibular second molars using cone-beam computed tomography. *Journal of Endodontics*, 47(12):1907–1916, 2021.
- [34] Nermin Morgan, Adriaan Van Gerven, Andreas Smolders, Karla de Faria Vasconcelos, Holger Willems, and Reinhilde Jacobs. Convolutional neural network for automatic maxillary sinus segmentation on cone-beam computed tomographic images. *Scientific Reports*, 12(1):1–9, 2022.
- [35] Matvey Ezhov, Maxim Gusarev, Maria Golitsyna, Julian M Yates, Evgeny Kushnerev, Dania Tamimi, Secil Aksoy, Eugene Shumilov, Alex Sanders, and Kaan Orhan. Clinically applicable artificial intelligence system for dental diagnosis with CBCT. *Scientific reports*, 11(1):1–16, 2021.
- [36] Jae-Hong Lee, Do-Hyung Kim, and Seong-Nyum Jeong. Diagnosis of cystic lesions using panoramic and cone beam computed tomographic images based on deep learning neural network. *Oral diseases*, 26(1): 152–158, 2020.
- [37] Mingjun Du, Xueying Wu, Ye Ye, Shuobo Fang, Hengwei Zhang, and Ming Chen. A combined approach for accurate and accelerated teeth detection on cone beam CT images. *Diagnostics*, 12(7):1679, 2022.
- [38] KS Lee, HJ Kwak, JM Oh, N Jha, YJ Kim, W Kim, UB Baik, and JJ Ryu. Automated detection of TMJ osteoarthritis based on artificial intelligence. *Journal of Dental Research*, 99(12):1363–1367, 2020.
- [39] Davood Karimi and Rabab Ward. A denoising algorithm for projection measurements in cone-beam computed tomography. *Computers in Biology and Medicine*, 69:71–82, 2016. ISSN 0010-4825.
- [40] Lianying Chao, Zhiwei Wang, Haobo Zhang, Wenting Xu, Peng Zhang, and Qiang Li. Sparse-view cone beam CT reconstruction using dual CNNs in projection domain and image domain. *Neurocomputing*, 493: 536–547, 2022. ISSN 0925-2312.

- [41] Yingzi Liu, Yang Lei, Tonghe Wang, Yabo Fu, Xiangyang Tang, Walter J Curran, Tian Liu, Pretesh Patel, and Xiaofeng Yang. CBCT-based synthetic CT generation using deep-attention cycleGAN for pancreatic adaptive radiotherapy. *Medical physics*, 47(6):2472–2483, 2020.
- [42] Berrylin J Ferguson. Fungus balls of the paranasal sinuses. *Otolaryngologic Clinics of North America*, 33(2):389–398, 2000.
- [43] Holger Scherl, Mario Koerner, Hannes Hofmann, Wieland Eckert, Markus Kowarschik, and Joachim Hornegger. Implementation of the FDK algorithm for cone-beam CT on the cell broadband engine architecture. In *Medical Imaging 2007: Physics of Medical Imaging*, volume 6510, pages 1666–1675. SPIE, 2007.
- [44] Willem Jan Palenstijn, K Joost Batenburg, and Jan Sijbers. The ASTRA tomography toolbox. In *13th International Conference on Computational and Mathematical Methods in Science and Engineering, CMMSE*, volume 2013, pages 1139–1145, 2013.
- [45] Kyung-Su Kim, Byung Kil Kim, Myung Jin Chung, Hyun Bin Cho, Beak Hwan Cho, and Yong Gi Jung. Detection of maxillary sinus fungal ball via 3-D CNN-based artificial intelligence: Fully automated system and clinical validation. *Plos one*, 17(2):e0263125, 2022.
- [46] Jing Chang and Jin Sha. An efficient implementation of 2D convolution in CNN. *IEICE Electronics Express*, 14(1):20161134–20161134, 2017.
- [47] Xuhua Ren, Lei Xiang, Dong Nie, Yeqin Shao, Huan Zhang, Dinggang Shen, and Qian Wang. Interleaved 3D-CNN s for joint segmentation of small-volume structures in head and neck CT images. *Medical physics*, 45(5):2063–2075, 2018.
- [48] Tianlin Liu, Anadi Chaman, David Belius, and Ivan Dokmanić. Learning multiscale convolutional dictionaries for image reconstruction, 2021.
- [49] Diederik P Kingma and Jimmy Ba. Adam: A method for stochastic optimization. *arXiv preprint:1412.6980*, 2014.
- [50] Mingxing Tan and Quoc Le. Efficientnet: Rethinking model scaling for convolutional neural networks. In *International conference on machine learning*, pages 6105–6114. PMLR, 2019.
- [51] Pieter-Tjerk De Boer, Dirk P Kroese, Shie Mannor, and Reuven Y Rubinstein. A tutorial on the cross-entropy method. *Annals of operations research*, 134(1):19–67, 2005.
- [52] Kaiming He, Xiangyu Zhang, Shaoqing Ren, and Jian Sun. Deep residual learning for image recognition. In *Proceedings of the IEEE conference on computer vision and pattern recognition*, pages 770–778, 2016.
- [53] Will Kay, Joao Carreira, Karen Simonyan, Brian Zhang, Chloe Hillier, Sudheendra Vijayanarasimhan, Fabio Viola, Tim Green, Trevor Back, Paul Natsev, et al. The kinetics human action video dataset. *arXiv preprint:1705.06950*, 2017.
- [54] Jun-Yan Zhu, Taesung Park, Phillip Isola, and Alexei A Efros. Unpaired image-to-image translation using cycle-consistent adversarial networks. In *Proceedings of the IEEE international conference on computer vision*, pages 2223–2232, 2017.



- [55] Junlin Han, Mehrdad Shoeiby, Lars Petersson, and Mohammad Ali Armin. Dual contrastive learning for unsupervised image-to-image translation. In *Proceedings of the IEEE/CVF Conference on Computer Vision and Pattern Recognition*, pages 746–755, 2021.
- [56] Javier Gurrola-Ramos, Oscar Dalmau, and Teresa E Alarcón. A residual dense U-Net neural network for image denoising. *IEEE Access*, 9:31742–31754, 2021. doi: 10.1109/ACCESS.2021.3061062.
- [57] Mufeng Geng, Xiangxi Meng, Jiangyuan Yu, Lei Zhu, Lujia Jin, Zhe Jiang, Bin Qiu, Hui Li, Hanjing Kong, Jianmin Yuan, et al. Content-noise complementary learning for medical image denoising. *IEEE Transactions on Medical Imaging*, 41(2):407–419, 2021.
- [58] Quan Huynh-Thu and Mohammed Ghanbari. Scope of validity of PSNR in image/video quality assessment. *Electronics letters*, 44(13):800–801, 2008.
- [59] Zhou Wang, Eero P Simoncelli, and Alan C Bovik. Multiscale structural similarity for image quality assessment. In *The Thrity-Seventh Asilomar Conference on Signals, Systems & Computers, 2003*, volume 2, pages 1398–1402. Ieee, 2003.
- [60] Gian Luca Fadda, Fabiana Allevi, Cecilia Rosso, Federica Martino, Carlotta Pipolo, Giovanni Cavallo, Giovanni Felisati, and Alberto Maria Saibene. Treatment of paranasal sinus fungus ball: A systematic review and meta-analysis. *Annals of Otology, Rhinology & Laryngology*, 130(11):1302–1310, 2021.
- [61] C Hodez, C Griffaton-Taillandier, and I Bensimon. Cone-beam imaging: Applications in ENT. *European annals of otorhinolaryngology, head and neck diseases*, 128(2):65–78, 2011.